Extreme Mechanics Letters 42 (2021) 101110

Contents lists available at ScienceDirect

Extreme Mechanics Letters

journal homepage: www.elsevier.com/locate/eml

Extreme deformations of the cantilever Euler Elastica under transverse aerodynamic load

Diego Misseroni [a,*,1], Ettore Barbieri [b,1], Nicola Maria Pugno [a,c]

[a] Laboratory of Bio-inspired, Bionic, Nano, Meta Materials & Mechanics, University of Trento, via Mesiano 77, I-38123 Trento, Italy
[b] Japan Agency for Marine-Earth Science and Technology (JAMSTEC), Research Institute for Value-Added-Information Generation (VAiG), Center for Mathematical Science and Advanced Technology (MAT), Computational Science and Engineering Group, Yokohama Institute for Earth Sciences (YES), 3173-25, Showa-machi, Kanazawa-ku, Yokohama-city, Kanagawa, 236-0001, Japan
[c] School of Engineering and Materials Science, Queen Mary University of London, Mile End Road, London, E1 4NS, UK

ARTICLE INFO

Article history:
Received 10 August 2020
Received in revised form 6 October 2020
Accepted 18 November 2020
Available online 1 December 2020

Keywords:
Follower forces
Euler Elastica
Large deformations
Flexible devices

ABSTRACT

Using an analytical solution of the Euler's *Elastica*, we stumbled upon peculiar shapes of a cantilever beam subject to a large value of shear follower force at the free end. Intrigued by whether such shapes existed or not, we set out to realise an experimental apparatus to validate our predictions. Attaining such system, in reality, is not at all a trivial task. Indeed, it has represented an experimental challenge for decades, due to the emergence of unstable configurations. After various attempts, we were finally able to conceive and realise a device capable of generating a transverse follower force to the beam via air-thrust. We compared the measurement of the forces and the deformation of the beam obtained experimentally with the analytical solution of the Euler's *Elastica* in dimensionless form. Since the experiments are quasi-static, the aerodynamic effect induced by the air flow are negligible; this is confirmed by the agreement between the experimental results and both theoretical and numerical predictions. During the experiments, we observed a high susceptibility to perturbations around a dimensionless load of 41.15. We used finite element simulations with an explicit time integration scheme to carry out a stability analysis. Our analysis confirmed the appearance of an unstable configuration for a load of 40.5. Therefore, by carefully tuning the apparatus, we could reach load values higher than the unstable load, at around 120. For such levels of forces, the solution of the *Elastica* prescribes hook-like shapes that we show experimentally in this paper. These results can find several applications, for instance, the design of soft-actuators, the realisation of more efficient drilling pipes for underwater, or underground, well or the design of biomedical equipment, such as catheters.

1. Introduction

Follower forces are a kind of non-conservative force whose direction depends on the deformation of the structure. Examples of follower forces in engineering are, for instance, the wind loading, the propulsive force of a rocket or the thrust induced by water flow on a garden hose. Extensive literature is available for tangential follower forces, although their existence is still the centre of an animose controversy [1], and their practical realisation challenged numerous researchers over the years. It is not our intent to participate in this debate; for the sake of this paper, we consider follower forces as useful abstractions for a variety of physical phenomena and engineering applications. Examples not just include structural mechanics, but cover rotordynamics and gyrodynamics [2], robotics and automatic control [3], aeroelasticity [4], fluid–structure interactions [5], smart materials [6], biomechanics [7], hydrodynamic peeling [8,9], cytoskeletal dynamics [10], molecular motors [11] and even astrophysics [12] and geophysics [13]. Follower forces fall under the more general umbrella of circulatory forces [14–16]. Even though only in recent years researchers framed follower forces into a more general and modern mathematical framework, early theoretical research on follower forces dates back to 1950. The most famous works include the Pflüger column [17–20], the Ziegler paradox [21–25], the Beck's column [26], the Reut's column problem [27,28], and the first monography on the stability of non-conservative forces due to Bolotin [29]. One of the most challenging issues related to the framework of follower forces was their actual realisation. Numerous researchers tried several attempts to realise follower forces experimentally through different methods. For instance, [30,31] used fluid flowing from a nozzle. The experimental setup proposed by [30] was used mainly to test mechanical systems made up of rigid bars (not of complaint elements), namely

* Corresponding author.
E-mail address: diego.misseroni@unitn.it (D. Misseroni).
[1] Both authors contributed equally.

https://doi.org/10.1016/j.eml.2020.101110
2352-4316/

with a finite number of degrees of freedom, suspended with some elastic springs. On the contrary, the setup by [31] was proposed to test flexible columns subject to tangential follower forces, but a huge nozzle box was mounted at the top of the beam. Instead, [32–34] used a solid motor rocket to induce follower forces on structures. Still, the non-negligible mass of the motor and the very short duration of the experiments made this method very complicated to be used. As correctly pointed out by Elishakoff in 2005 [1], none of the methods correctly realised a tangential follower force as postulated in the Ziegler column problem. A significant breakthrough was achieved in 2011 by [35], who designed and tested a device capable of realising a follower tangential force exploiting dry friction. The idea consists of mounting a freely rotating wheel at the top of the beam constrained to slide against a moving surface. In this paper, instead, we present the experimental realisation of a cantilevered rod under large shear follower forces at the free tip (Fig. 1a). The problem is very complicated as the investigation of the hook-like shape of the *Elastica* produced by the orthogonal follower force requires that the angle included between the applied force vector and the axis of the unformed configuration $\in [-\pi, \pi]$. We realised a setup that provided an "approximate" follower force to the beam via air-thrust, as the experimental setup proposed by [35] cannot be used. Being aware that this method introduces some complication in the modelling, we carefully tuned the pressure of the air flow to reduce as much as possible the spurious effects associated with the fluid/structure interaction. We have validated the experimental apparatus by estimating most of the discrepancies between the theoretical model and the experiments. Among these the main are (i) friction between the beam and the substrate, (ii) frictional dissipation along the tube, (iii) sudden changes in flow area, (iv) stiffening of the deformable tube due to the internal air pressure. By contrast to the Herrmann setup, we have been able to avoid the presence of the nozzle, to lower the required air pressure to deform the mechanical system and to remove the two suspending cables that can change the deformed *Elastica* dramatically. To assess the goodness of the experimental setup, we compared the deformation with an analytical solution of the *Elastica*. The excellent agreement between the experimental results and both theoretical and numerical predictions suggests that, in this specific kind of experiments, the provided orthogonal force is an acceptable approximation of a follower force. Even though analytical solutions already exist [36], here we provide a reformulation of the *Elastica* in terms of the curvatures [37]. This reformulation has one significant advantage. The phase-portrait of this equation leads to discover the spatial periodicity of the solution that explains the loop-like appearance of its shapes. Multiple loops are known to appear in the *Elastica* with fixed forces [38]: we show in this paper how similar shapes emerge *mutatis mutandi* also for rods loaded by follower forces. Also, we performed Finite Element (FE) simulations to capture the instability onset. The use of FE is necessary since systems loaded by follower forces do not admit a potential of the type *Strain Energy-External Work* [16,39] since follower forces are non-conservative. The external work done by such a kind of forces is path-dependent and a non-zero work can be extracted in a closed path, as shown in Fig. 1(b). Thus, a stability analysis based on the study of the second variation of the Lagrangian cannot be used. Although the experimental setup presented in this article could be further improved, the observed outcomes can find application in several fields. For instance, these results can play a crucial role in the description and in the understanding of pressure-fed compliant mechanisms (e.g. in the design of soft-actuators). To increase the positioning precision or to achieve more complicated shapes, a pneumatically pressurised soft robot arm could be realised with one or more small voids that open and close on demand. Such a mechanism could be exploited to compensate for the dynamic effect that can reduce repeatability and accuracy of movements. Moreover, hook-shaped configurations could permit to fold/unfold a compliant mechanism and thus penetrate narrow spaces. The present experimental setup could be used to realise more efficient flexible devices and better understand, for instance, the deformation mechanism.

2. Material and methods

2.1. Experimental apparatus

The experimental setup, shown in Fig. 1(c), was specifically designed to apply a tunable transverse follower force at the top of the beam. The actual realisation of a follower force acting on a structure has always been considered a very complicated problem. A straightforward way to provide this kind of force to a system is to exploit the reaction force generated by a fluid (air) flowing from a small circular void orthogonal to the beam axes as reported in the inset (a) of Fig. 1b. The void (diameter d_{out}=0.8 mm) was realised by a 0.8 mm in diameter biopsy punch. A very flexible silicone tube of length L_{tube}=170 mm and weight P_{tube}=13.8 mN, inner and outer diameters d_{int}=1.5 mm and d_{ext}=2.5 mm, respectively, is used in the experiments. The clamped end of the flexible tube is fixed to a rigid metal tube where the air that produces the shear force flows. During the experiments, the applied shear follower force is linearly increased by changing the air flow immediately upstream of the flexible tube. The air pressure, and accordingly the end-thrust, was raised through a solenoid valve (pressure gauge, internal diameter d_{in}=8 mm) connected to a NI CompactRio acquisition system. A LabVIEW algorithm permitted to adjusts the air flow to a wanted value via a closed-loop control. The pressure rate was always kept under 0.04 bar/s, and to overcome instabilities, we had to carefully reduce and tune it manually. An air condensate filter was mounted before the pressure gauge for draining condensate and for cleaning the air. The whole apparatus, arranged horizontally to prevent the gravitational effect, is mounted on an optical table (Nexus from ThorLabs). A Teflon (PTFE) sheet was also used to reduce the friction between the experimental support and the flexible beam. A friction coefficient (μ_f) Silicon on PTFE (Teflon) surface of about 0.48 $\pm$ 0.05 has been estimated via specific frictional experiments. Five preliminary tension tests were performed on the silicone tube to determine its mechanical properties. A mean value of 12.95 MPa was estimated for the Young's modulus (E) of the tube by analysing the stress–strain curves recorded during these experiments. The effect of the air pressure on the bending stiffness of the tube was estimated through an indirect method as explained in Section 4.1. Alongside the execution of the experiments, pictures were taken by a Sony Alpha 6300 camera whereas movies were taken with a Sony PXW-FS5 video camera (30 fps).

2.2. Numerical and theoretical methods for the deformation and instabilities

Abaqus simulations were performed with the purpose to confirm the theoretical findings and complementing the experiments. The circular elastic rod, clamped at one end and subject to the transversal follower force at the other end, was modelled with about 400 2D beam elements (B23). The same geometrical and mechanical properties used in the experiments were also considered in the simulations to approximate the real behaviour of the structure better. Two types of simulations were carried out to mimic the experiments. In one case, Dynamic/Explicit simulations were performed to capture the first instability onset. In

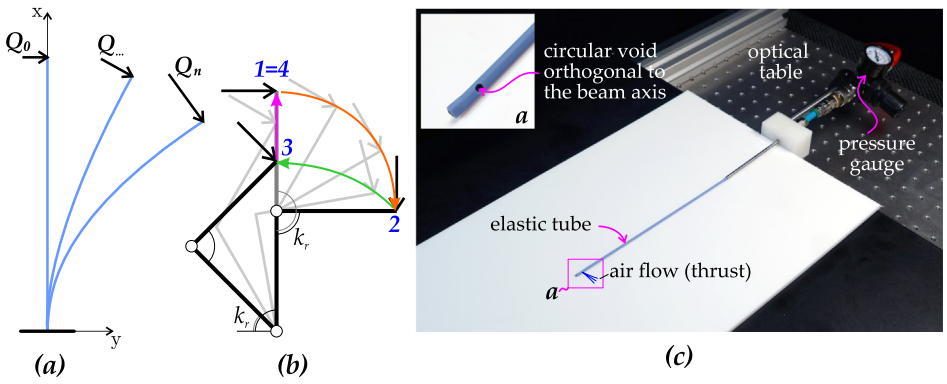

Fig. 1. (a) The scheme of the problem. (b) A 2 degree-of-freedom structure, made up of 2 rigid bars connected by elastic hinges, is subject to an orthogonal follower force. The external work done by such force is path-dependent and therefore a positive work can be extracted in a closed path (1→2→3→4) [39]. (c) The experimental setup exploited in the experiments. The transverse follower force is provided to the end of the cantilever tube by a fluid (air) flowing from a small void orthogonal to the beam axis.

the other case, Static Riks Analysis were exploited to circumvent instabilities and achieve large deformation. A similar approach was also used experimentally by carefully tuning the pressure of the air flowing from the small circular void orthogonal to the beam axis. The applied load was increased very smoothly (Smooth-step type) as done experimentally.

3. Theory

The equations of equilibrium of forces and moments of a bent, unshearable and inextensible elastic rod are [40,41]

$$Q' - \mu N - q = 0, \quad N' + \mu Q = 0, \quad M' - Q = 0, \tag{1}$$

where $(\cdot)' = \mathrm{d}/\mathrm{d}S$ with S being the arc length, Q is the shear force, μ is the curvature, N is the axial force, M is the bending moment and q is a distributed normal load. The kinematics of the elastica is given by

$$\theta' = \mu, \quad x' = \cos\theta, \quad y' = \sin\theta, \tag{2}$$

with θ being the rotation and x and y the Cartesian coordinates. We further assume a linear elastic constitutive model, a homogeneous material and uniform cross-section along the whole rod

$$M = E\,I\,\mu, \tag{3}$$

with E the Young modulus and I the second moment of area of the cross-section. We now introduce the following dimensionless variables

$$S^* = \frac{S}{L}, \qquad \mu^* = \mu\,L, \tag{4}$$

with L being the length of the rod. We obtain the following dimensionless variables for the boundary conditions, where $(\cdot)_0$ refers to variables at $S = 0$

$$M_0^* = \frac{M_0\,L}{E\,I}, \qquad Q_0^* = \frac{Q_0\,L^2}{E\,I}, \qquad N_0^* = \frac{N_0\,L^2}{E\,I}, \qquad q^* = \frac{q\,L^3}{E\,I}, \tag{5}$$

with M_0 being a moment applied to the free end, Q_0 a terminal shear force, N_0 an applied terminal axial force and q a distributed load. Eqs. (1) can be combined in the single equation

$$\mu'' + \frac{1}{2}\mu^3 - A\,\mu - q = 0, \tag{6}$$

with

$$A = N_0 + \frac{1}{2}{\mu_0}^2. \tag{7}$$

In the equation above, μ_0 is an applied curvature or bending moment at the free end of the rod. We have removed the $(\cdot)^*$ *for ease of reading*. Multiplying both sides of Eq. (6) by μ' and considering q uniform (independent from S), after integrating between 0 and S we obtain

$${\mu'}^2 + \frac{\mu^4}{4} - A\,\mu^2 - 2\,q\,\mu = B, \tag{8}$$

with

$$B = {N_0}^2 + {Q_0}^2 - A^2 - 2\,\mu_0\,q. \tag{9}$$

Eq. (8) is the most general form that includes all the possible boundary conditions. We consider $\mu_0 = N_0 = q = 0$, therefore we get

$${\mu'}^2 = -\frac{\mu^4}{4} + {Q_0}^2. \tag{10}$$

3.1. Calculation

The phase portrait of Eq. (10) is shown in Fig. 2a. By examining such plot, we find *a priori* some properties of the solution $\mu(S)$ (Fig. 2b). For example, the $\mu - \mu'$ curve is closed, which means that the solution $\mu(S)$ must be periodic in space, with period $4\,S_{\max}$, and oscillates between $-\mu_{\max}$ and $\mu_{\max}$. Also, five points of the solution are known. The first one is the initial condition $\mu(0) = 0$ with initial slope $\mu' = \mu'_{\max} = Q_0$ equal to the maximum possible slope. Assuming that $Q_0 > 0$, the solution proceeds clockwise from the initial condition. The second known point is a maximum for $S = S_{\max}$, where $\mu' = 0$ and $\mu = \mu_{\max}$; the third one is a zero of the solution at $S = 2\,S_{\max}$ with maximum negative slope $-\mu'_{\max}$; the fourth point is a minimum for $S = 3\,S_{\max}$, where $\mu' = 0$ and $\mu = -\mu_{\max}$; finally, the last known point is a zero at $S = 4\,S_{\max}$ with slope $\mu'_{\max}$. Because of the double symmetry of the phase portrait (Fig. 2a), $\mu_{I-II} = -\mu_{III-IV}$ and μ_I and μ_{II} are symmetric with respect to the μ axis. The value of $\mu_{\max}$ can be easily computed from Eq. (10) by setting $\mu' = 0$

$$\mu_{\max} = \sqrt{2\,Q_0}, \tag{11}$$

while the value of $\mu'_{\max}$ is obtained from Eq. (10) by setting $\mu = 0$

$$\mu'_{\max} = Q_0. \tag{12}$$

The full details of the solution of Eq. (10) can be found in Appendix A. We recall here the main results. The solution $\mu(S)$ is a periodic solution with quarter-period $S_{\max}$ that oscillates between $-\mu_{\max}$ and $\mu_{\max}$

$$S_{\max} = \frac{2\,K(-1)}{\mu_{\max}} = \sqrt{\frac{2}{Q_0}}\,K(-1), \tag{13}$$

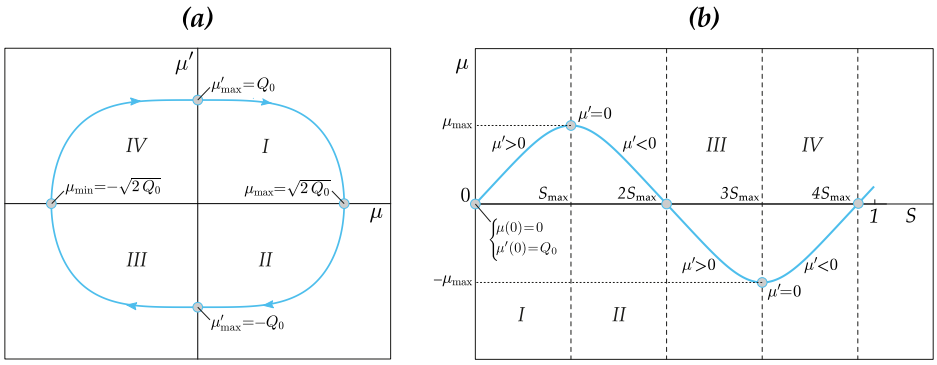

Fig. 2. Phase portrait of Eq. (10) and curvature $\mu(S)$. (a) Phase portrait with $Q_0 > 0$: the solution $\mu(S)$ is periodic in space. The dots are points of the solution, known *a priori*. Also, the solution has a double symmetry with respect to axes μ and μ'. (b) The four stages of the solution $\mu(S)$.

with $K(-1)$ being the *complete elliptical integral of the first kind* of argument -1. Let us then normalise the curvature and the curvilinear abscissa

$$\bar{S} = \frac{S}{S_{\max}}, \qquad \bar{\mu} = \frac{\mu}{\mu_{\max}}. \tag{14}$$

The solution is then

$$\bar{\mu}(\bar{S}) = \mathrm{sn}\left(K(-1)\bar{S}|-1\right), \tag{15}$$

$$\bar{\mu}'(\bar{S}) = K(-1)\,\mathrm{cn}\left(K(-1)\bar{S}|-1\right)\,\mathrm{dn}\left(K(-1)\bar{S}|-1\right), \tag{16}$$

with sn, cn and dn being respectively *Jacobi sn, cn and dn elliptic functions*.

The rotation is

$$\theta(S) = \beta_1 - \beta(S), \qquad \beta_1 = \beta(1) = \theta_0, \tag{17}$$

with

$$\beta(\bar{S}) = \arcsin\left(\bar{\mu}^2\right)\,\mathrm{sign}\left(\bar{\mu}'\right) + \pi\,\left(n_{\downarrow}(\bar{S}) - n_{\uparrow}(\bar{S})\right), \tag{18}$$

where $n_{\downarrow}(\bar{S})$ is the number of times μ' changes sign *from positive to negative* between 0 and $\bar{S}$, while $n_{\uparrow}(\bar{S})$ is the number of times μ' changes sign *from negative to positive*

$$n_{\downarrow}(\bar{S}) = 1 + \left\lfloor \frac{\bar{S}-1}{4} \right\rfloor, \quad n_{\uparrow}(\bar{S}) = 1 + \left\lfloor \frac{\bar{S}-3}{4} \right\rfloor, \tag{19}$$

where

$$\lfloor x \rfloor = x - \{x\}, \tag{20}$$

with $\{x\} =$ mod $(x, 1)$ and mod being the module function.

The deformation is

$$\begin{aligned} x(\bar{S}) &= 1 - I_{c_\theta}(\bar{\mu}_1) + I_{c_\theta}(\bar{\mu}), \\ y(\bar{S}) &= -I_{s_\theta}(\bar{\mu}_1) + I_{s_\theta}(\bar{\mu}), \end{aligned} \tag{21}$$

with

$$\begin{aligned} I_{c_\theta} &= \cos\beta_1 I_{c_\beta}(\bar{\mu}) + \sin\beta_1 I_{s_\beta}(\bar{\mu}), \\ I_{s_\theta} &= \sin\beta_1 I_{c_\beta}(\bar{\mu}) - \cos\beta_1 I_{s_\beta}(\bar{\mu}), \end{aligned} \tag{22}$$

and

$$\begin{aligned} I_{c_\beta} &= \sqrt{\frac{2}{Q_0}}\,\bar{\mu}, \\ I_{s\beta} &= \sqrt{\frac{2}{Q_0}}\,\left(\mathrm{sign}\left(\bar{\mu}'\right)\,I_2(S) + 2\,I_2(1)\,\left(n_{\downarrow} + n_{\uparrow}\right)\right). \end{aligned} \tag{23}$$

In the previous equation

$$I_2(\bar{\mu}) = \int_0^{\bar{\mu}} \frac{\bar{\mu}^2}{\sqrt{1-\bar{\mu}^4}}\mathrm{d}\bar{\mu} = E(\arcsin\bar{\mu}\mid -1) - F(\arcsin\bar{\mu}\mid -1), \tag{24}$$

where E is the *elliptic integral of the second kind* and F is the *elliptic integral of the first kind* not to be confused with the Young's Modulus.

4. Results and discussion

By using the aforementioned experimental setup, we executed both qualitative and quantitative experiments to test the validity of the proposed theoretical model. Eventually, specific experiments were executed to capture the unstable mode of the cantilever beam. To compare the theory with the experiments the relation between the pressure p_{in} and the follower thrust $Q_{exp,th}$ acting at the top of the beam has been derived exploiting the *continuity equation*, the *momentum equation* and the *energy equation* on each Control Volume Element (CVE) reported in Fig. 6a. Such a relation has been determined for: (i) the ideal case with no-dissipations and (ii) the real case with the presence of all the sources of dissipation such as the wall friction and the sudden contraction of the flow area. The pressure/thrust relation is given in a closed-form expression for the ideal case, Eq. (68). When the dissipations are introduced into the model, a specific numerical algorithm has been developed to compute iteratively the mass flow and, thus, the generated end thrust. For a specific value of the recorded pressure, the discrepancy between the follower thrust $Q_{exp,th}$ for the ideal case (black/dashed line in Fig. 6b) and the real case (black/continuous line in Fig. 6b) gives a quantitative assessment of the mass flow losses affecting the experiments. In the investigated pressure range, the average decrease of the follower thrust associated to mass flow losses is of about 9.35% $\pm$ 3.79% with a minimum value of 5.91% for a pressure of 2 bar. It is worth to mention that the mass flow losses are in percentage higher for low pressure. The relation between the transversal follower force $Q_{exp,th}$ and the air pressure p_{in}, expressed by Eq. (67), is of the type $Q_{exp,th} \propto k p_{in}^c$, with $k \in \Re$ and $1 < c < 2$. In the previous expression, the non-linear behaviour is related to the fact that air is a compressible fluid whose density and temperature deeply depend on the pressure. In fact, if the fluid was incompressible, such as water, the relation between $Q_{exp,th}$ and the air pressure p_{in} would be linear. See Appendix B for the details.

4.1. Quasi-static experiments

The comparison between theory and experiments was accomplished as follows. First, a deformed configuration of the structure was computed analytically integrating the equation of the *Elastica* for increasing values of the follower force, Q_{theory}. Then, the follower thrust $Q_{exp,th}$, function of the air pressure, needed in the

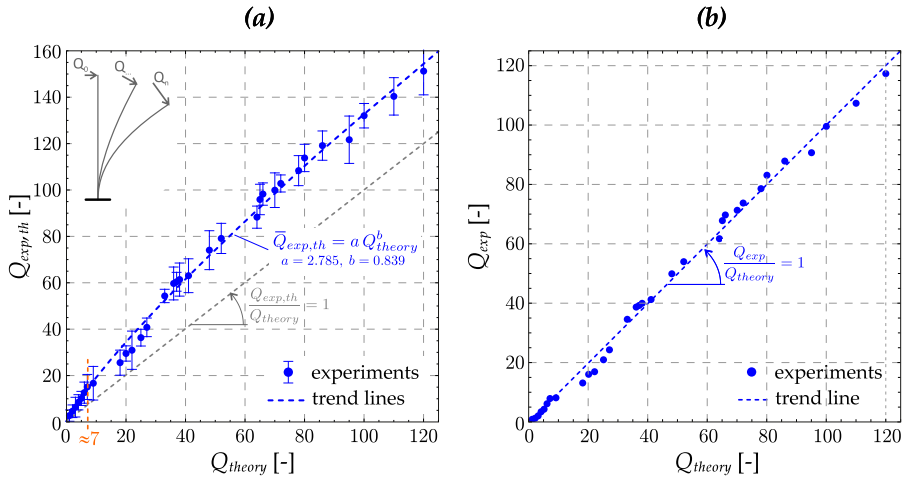

Fig. 3. Relation between the (dimensionless) theoretical and experimental transverse force that produce the same deformed configuration of the structures. Each marker refers to different deformed configurations. (a) Relation between Q_{theory} and $Q_{exp,th}$. The blue/dashed line represents the non-linear best-fit curve defined by the 2-parameters model (Eq. (25)). The slope change attained at $Q_{theory} \approx 5-7$ (orang/dashed line) could be assumed as a threshold for which the present experimental apparatus provides inaccurate or accurate results. (b) Relation between Q_{theory} and the actual force Q_{exp} produced at the top of the beam (computed accordingly with Eq. (27)). In this case, the results can be well represented by a straight line with slope 1. (For interpretation of the references to colour in this figure legend, the reader is referred to the web version of this article.)

experiments to match the predicted deformed configuration (for each of the given Q_{theory}) was evaluated. In Fig. 3a, each of the blue/disk markers depicts the relation between the (dimensionless) theoretical, Q_{theory}, and experimental, $Q_{exp,th}$, follower force that yields to the same deformed configuration of the structures. In the graph, the markers and their relative bars represent, respectively, the mean value and the standard deviation of the results collected performing four different experiments.

If theory and experiments were in perfect agreement, each $Q_{exp,th}$ estimated experimentally would be equal to the corresponding Q_{theory} imposed to solve the equation of the *Elastica*. Therefore, the experimental results depicted in Fig. 3a should be well fitted with a straight line of slope 1. Instead, a two-parameters non-linear model of the type

$$\overline{Q}_{exp,th} = a\,Q^{b}_{theory}, \quad \text{where } a \approx 2.785,\ b \approx 0.839, \tag{25}$$

represents the best fit for the experimental data reported in Fig. 3a over the whole investigated Q_{theory} range. In the previous equation, $\overline{Q}_{exp,th}$ represents the value of $Q_{exp,th}$ provided by the non-linear fit (blue/dashed line in the figure). As expected, the experimental results show some deviation from ideality. Firstly, a larger force is needed in the experiments to achieve the deformed configurations computed theoretically at first. Since the air flow dissipations have been taken into account in the calculation (Appendix B), the discrepancy between $Q_{exp,th}$ and Q_{theory} has to be referred mainly to (i) the tube/substrate interaction and to (ii) the flexural rigidity increase due to the internal air pressure. In fact, the *Elastica* has been solved neglecting the friction between the tube and the substrate and considering a constant bending stiffness EI for the flexible tube, namely independent from the internal air pressure. Hence, a $Q_{exp,th}$ greater than Q_{theory} is required in the experiments to overcome friction (that always opposes the motion) and to deform the flexible tube which stiffens as the internal air pressure increases. The order of magnitude of friction effect was determined via the following approximate calculation. The resultant friction force, $\widehat{R}_f$, that opposes to motion is $\mu_f\, P_{tube}$=6.62×10^{-3} N which correspond to a dimensionless $R_f = \widehat{R}_f L^2_{tube}/(EI) \approx 8$. Such a resultant force acts at $L_{tube}/2$ and generates a reactive couple $R_f L_{tube}/2$ at the clamped end of the tube. For simplicity, we have imagined frictional effect equivalent to a concentrated force Q_f acting at the top of the beam that reduces the applied air-thrust. This force, equal to $Q_f R_f/2$, was determined by imposing the equivalence between the generated reactive couples at the clamped end of the beam, namely $R_f L_{tube}/2 = Q_f L_{tube}$. Of course, this value is purely indicative as it is realistic only at the beginning of the experiments when the tube is almost straight. In fact, the very complicated shapes assumed by the *Elastica* undergoing large deformations lead to a non-constant reactive couple (evaluated at the clamped end of the tube) as the beam deforms. Hence, the effect of friction, that opposes to motion, is not constant during the evolution of the experiments. Moreover, we have observed that the applied end-thrust does not remain entirely on the plane of motion but tends to assume a slightly out-of-plane direction. This aspect leads to the occurrence of the stick–slip phenomenon. To provide an exact quantification of this phenomenon is not a trivial task. We have decided to take this into account through a concentrated force applied at the free end of the same order of magnitude of previously determined Q_f, namely $Q_{stick-slip} \approx 4$. Eventually, friction and stick–slip have been assumed equivalent to a $Q_{fric,tot} = Q_f + Q_{stick-slip} \approx 8$, acting at the top of the flexible tube that opposes motion. Assuming for simplicity constant and equal to $Q_{fric,tot} \approx 8$ the detrimental effect of friction and stick–slip, we have decided to combine the remaining discrepancies between the theoretical model and the experiments into a non-constant coefficient $\eta(p_{in})$ that counts the bending stiffness increase due to internal air pressure. Such a coefficient permits to define an effective dimensionless end-thrust $Q_{exp,ef}$ as a function of an effective elastic modulus $E(p_{in}) = \eta(p_{in})E$,

$$Q_{exp,ef} = \frac{Q_{exp,th}}{\eta(p_{in})} = \frac{\widehat{Q}_{exp,th}L^2}{\eta(p_{in})EI} = \frac{\widehat{Q}_{exp,th}L^2}{E(p_{in})I}, \tag{26}$$

where $\widehat{Q}_{exp,th}$ is the dimensional end-thrust. The experimental follower end-thrust purified from all the dissimilarities between the theoretical model and the experiments (friction between the beam and the substrate, frictional dissipation along the tube, sudden changes in flow area, bending stiffness increase due to air pressure) is estimated via the relation

$$Q_{exp} = \frac{Q_{exp,th}}{\eta(p_{in})} - Q_{fric,tot}. \tag{27}$$

Each η_i value is determined in post-processing by exploiting the trend line (Eq. (25)) and by imposing $Q_{exp,i} = Q_{theory,i}$ in Eq. (27)

Table 1
Comparison between the (dimensionless) theoretical values of the follower force (Q_{theory}) and the actual follower force (Q_{exp}) estimated in the experiments to achieve the deformed shapes reported in Fig. 4 and calculated via Eq. (27).

Subfigure	1	2	3	4	5	6	7	8	9	10
Q_{theory}	0	1	2	20	27	36	52	78	95	120
Q_{exp}	0	0.88	1.26	16.05	24.30	38.69	53.99	78.59	90.70	117.34

as

$$\eta_i(p_{in,i}) = \frac{\overline{Q}_{exp,th,i}}{Q_{theory,i} + Q_{fric,tot}}, \tag{28}$$

where $\overline{Q}_{exp,th}$ represents the value of $Q_{exp,th}$ provided by the trend line. The coefficient $\eta(p_{in})$, estimated by Eq. (28), ranges between $\approx$ 1 (p_{in}= 0.18 bar) and $\approx$ 1.24 (p_{in}= 1.8 bar). Indeed, such coefficient provides just an estimate of the flexural rigidity increase due to internal pressure since it has been determined by an indirect method. In Fig. 3b, the (dimensionless) theoretical values of the follower force (Q_{theory}) are compared with the actual mean value of the follower force (Q_{exp}) produced at the top of the beam and computed by applying Eq. (27). In this case, it can be observed that the markers are well-fitted by a straight line with slope 1. This means that now theory and experiments are in good agreement.

In Fig. 4 the snapshots of deformed *Elastica* as observed in the experiments (frames extracted from the movies taken during a test) are superimposed to those predicted by the mathematical model (red/dashed lines). The deformed shapes depicted in the sub-figures and labelled from 1 to 10 refer to an increasing transverse force applied at the top of the beam. The results shown in Figs. 4 and 5 suggest a $Q_{theory} \approx 5$ as a threshold value for which the present experimental apparatus provides inaccurate or accurate results. In fact, from this value onwards, the deformed shapes observed experimentally start to coincide with those predicted theoretically (Fig. 5). Such a value almost agrees with the marked change of slope of the experimental trend line attained at $Q_{theory} \approx 7$, as shown in Fig. 3a (orange/dashed line).

In the same figure, it is also reported the deformed configurations obtained through FE Static Riks analysis (green/continuous line). By observing the photos, we highlight how the theory slightly differs from the experiments in the first snapshots (2 and 3). This problem is manly due to the friction and stick–slip between the silicon tube and the Teflon sheet that is in percentage higher for low value of the applied air-thrust. In fact, at the beginning of the test the applied force is small if compared to the friction force. From the fourth snapshots forward the experiments definitely substantiate the theoretical prediction and the numerical findings. From the figures, we can appreciate the appearance of the deformed hook-shaped configurations for Q greater than 20. The matching is almost perfect for Q ranging from about 35 to 100 where the hook-like shapes are coincident with those predicted theoretically and numerically. For Q higher than 100 a slight discrepancy between experiments and theory is revealed (tenth snapshot). By manually tuning the pressure gauge of the experimental apparatus, we were able to overcome the first unstable mode that appears at about $Q \approx 41$ and reaching relative extreme deformations of the rod up to (dimensionless) loads of 120. In conclusion, the comparison between the deformed structure captured during a test, the theoretical prediction and the FE results, shown in Fig. 4, reveals a globally good agreement. A record of a quasi-static experiment and its comparison with numerical and theoretical predictions is provided as supplementary material.

Table 1 shows the comparison between the (dimensionless) theoretical values of the follower force (Q_{theory}) and the actual follower force (Q_{exp}) computed through Eq. (27) to achieve the shapes reported in Fig. 4.

4.2. Stability experiments

The same experiments reported in Fig. 4 were repeated to capture the unstable mode of the cantilever beam, as predicted from the numerical simulations. Such results are shown in Fig. 5. In these experiments, the pressure of the air flowing from the small circular void was simply increased linearly without any particular tuning expedient. The deformed shapes depicted in the sub-figures and labelled from 1 to 5 refer to an increasing transverse force applied at the top of the beam. From the second to the fourth snapshot, the experiments are in good agreement with theoretical predictions, as observed in the quasi-static experiments. As discussed in detail in Section 4.1, the trend line reported in Fig. 3a shows a marked change of slope at a value of $Q \approx 7$. This peculiarity seems to represent the transition from which the deformed shapes observed experimentally start to coincide with those predicted theoretically. Therefore, such a value could be assumed as the lower limit for which the experimental apparatus provides accurate results. The numerical solution revealed that an unstable mode appears at $Q_0 = 40.5$ against a $Q_0 = 41.15$ observed in the experiments. The fifth snapshot shows the appearance of the first instability mode. The instability onset was estimated both numerically and experimentally following the same criterion. The adopted method consists in comparing subsequent frames extracted from the record of the experiments (or of the simulations). We have assumed as the instability onset the value of Q such that from this value onwards four subsequent frames exhibit dynamic oscillations characterised by a monotonically increasing amplitude. A record of an experiment performed to capture the instability onset, and its comparison with numerical prediction is provided as supplementary material.

5. Conclusions

In this paper, we presented a device capable of creating an "approximate" perpendicular follower force. Unfortunately, the complexity of this problem prevents the exploiting of the Bigoni and Noselli [35] setup that would produce a "nearly" perfect follower force as thought by Ziegler. The rig consists of a flexible silicone tube with a circular opening at the free end. A pressure gauge provides air flow to the fixed end — the thrust generated by the outflow results in a shear follower force. The motivation behind the design of such apparatus was the appearance of charming deformations of a cantilever rod subjected to a shear follower force. In particular, the closed-form solution of the *Elastica* (derived in this paper) showed fascinating shapes at relatively high loads. By *relatively*, we mean a shear force Q_0 normalised to the bending stiffness EI of the rod, meaning $Q_0L^2/(EI)$, with L being the length of the rod. At high loads, $Q_0 > 10$, the analytical solution dictates a deformation that seems hook-like, with spatial dimensionless frequency $1/S_{\max}$ increasing with the load to a law $Q_0^{1/2}$ (from Eq. (13)). The deformed shapes predicted theoretically were compared with those obtained by performing both quasi-static experiments and Riks numerical simulations. Such a comparison showed a good agreement between experiments, FE simulations and theory. Finally, stability experiments were carried to capture the first instability mode of the flexible beam. Moreover, an explicit finite-element calculations were performed in Abaqus to verify the instability onset determined experimentally. The setup presented in the article can find application in several fields. For instance, these results can play a key role in the description and in the understanding of pressure-fed compliant mechanisms (e.g. in the design of soft-actuators), in the realisation of more efficient drilling devices or in the design of biomedical equipment, such as catheters.

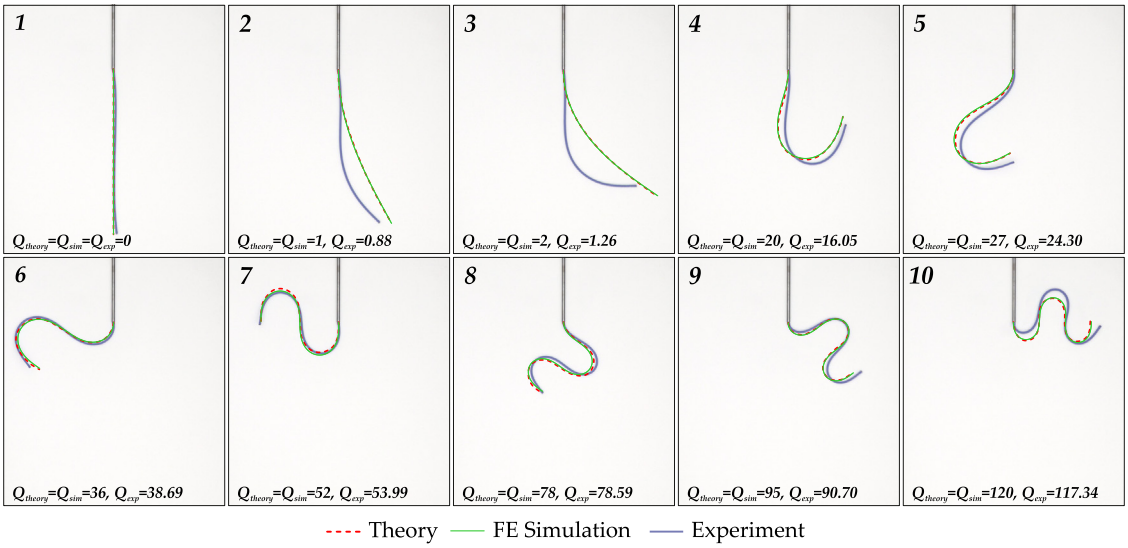

Fig. 4. The *Elastica* as predicted from the theory (red/dashed line) is superimposed to experiments (blue/continuous line) and FE results (green/continuous line). In this case, a Riks analysis was performed in Abaqus to circumvent instabilities and achieve large deformations. Each sub-figure, labelled from 1 to 10, refers to an increasing follower shear force acting at the top of the beam. (For interpretation of the references to colour in this figure legend, the reader is referred to the web version of this article.)

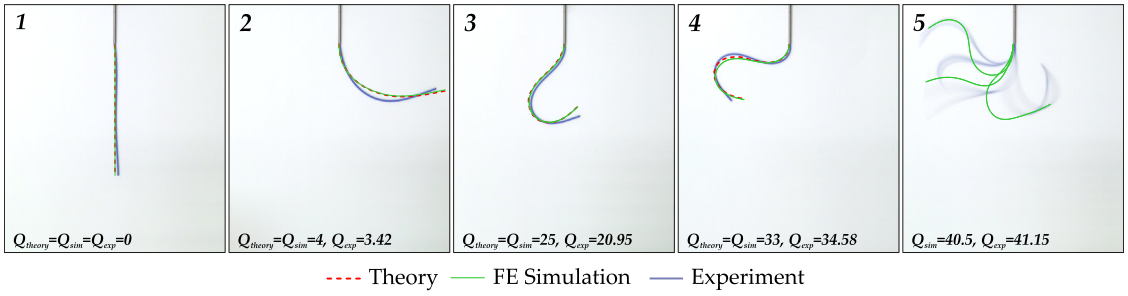

Fig. 5. The *Elastica* as predicted from the theory (red/dashed line) is superimposed to experiments (blue/continuous line) and FE results (green/continuous line). In this case, a Dynamic/Explicit analysis was performed in Abaqus to capture the unstable mode. Each sub-figure, labelled from 1 to 5, refers to an increasing follower shear force acting at the top of the beam. (For interpretation of the references to colour in this figure legend, the reader is referred to the web version of this article.)

Declaration of competing interest

The authors declare that they have no known competing financial interests or personal relationships that could have appeared to influence the work reported in this paper.

Acknowledgements

D.M. and N.M.P are supported by the Italian Ministry of Education, University and Research (MIUR) under the "Departments of Excellence" grant L. 232/2016, the ARS01-01384-PROSCAN grant and the PRIN 2017 20177TTP3S grant. The authors are grateful to Eng. F. Vinante for the assistance during the experiments and to Dr. M. Redolfi for the stimulating discussion.

Appendix A. Analytical solution of the elastica under a terminal shear follower force

A.1. Curvature

Assuming $0 \leq S \leq S_{\max}$ and $Q_0 > 0$, Eq. (10) can be written as

$$\frac{\mathrm{d}\mu}{\sqrt{1-\bar{\mu}^4}} = Q_0\,\mathrm{d}S, \tag{29}$$

where $\bar{\mu} = \mu/\mu_{\max}$. Let us consider the normalised variable $\bar{S} = S/S_{\max}$, with the exact expression of $S_{\max}$ still unknown at this stage: Eq. (29) becomes

$$\frac{\mathrm{d}\bar{\mu}}{\sqrt{1-\bar{\mu}^4}} = \frac{1}{2}\,\mu_{\max} S_{\max}\,\mathrm{d}\bar{S}. \tag{30}$$

By integrating both sides between 0 and respectively μ and S we obtain

$$F(\arcsin\bar{\mu}, -1) = \frac{\mu_{\max} S_{\max}}{2}\,\bar{S}, \tag{31}$$

where $F(\varphi, k)$ is the *incomplete elliptic integral of the first kind*. Inverting equation (31), we get

$$\bar{\mu}(\bar{S}) = \mathrm{sn}\left(\frac{\mu_{\max} S_{\max}}{2}\,\bar{S}\middle|-1\right), \tag{32}$$

where sn is the *Jacobi sn elliptic function*. The quarter-period of the sn function is given by the *complete elliptic integral of the first kind* $K(-1)$, therefore

$$S_{\max} = \frac{2\,K(-1)}{\mu_{\max}} = \sqrt{2}\,K(-1)\,Q_0^{-1/2} \approx 1.8541\,Q_0^{-1/2}. \tag{33}$$

To summarise

$$\bar{\mu}(\bar{S}) = \mathrm{sn}\left(K(-1)\,\bar{S}\middle|-1\right), \tag{34}$$

$$\bar{\mu}'(\bar{S}) = K(-1)\,\mathrm{cn}\left(K(-1)\bar{S}|-1\right)\ \mathrm{dn}\left(K(-1)\bar{S}|-1\right), \tag{35}$$

with cn and dn being respectively *Jacobi cn and dn elliptic functions*. The differential relationship between $\bar{\mu}$ and $\bar{S}$ is

$$\mathrm{d}\bar{S} = \frac{1}{K(-1)}\ \mathrm{sign}\left(\bar{\mu}'\right)\ \frac{\mathrm{d}\bar{\mu}}{\sqrt{1-\bar{\mu}^4}}. \tag{36}$$

A.2. Rotation

With boundary condition $\theta(1) = 0$, the rotation is given by

$$\theta(S) = \int_S^1 \mu(S)\,\mathrm{d}S = \int_0^1 \mu(S)\,\mathrm{d}S - \int_0^S \mu(S)\,\mathrm{d}S = \beta_1 - \beta(S), \tag{37}$$

where

$$\beta(S) = \int_0^S \mu(S)\,\mathrm{d}S \qquad \beta_1 = \beta(1). \tag{38}$$

The integral of the curvature in S can be computed as follows

$$\beta(S) = \mu_{\max} S_{\max} \int_0^{\bar{S}} \bar{\mu}\,\mathrm{d}\bar{S} = 2\,K(-1)\ \int_0^{\bar{S}} \bar{\mu}\,\mathrm{d}\bar{S}. \tag{39}$$

Using Eq. (36)

$$\beta(\bar{S}) = 2\int_0^{\bar{\mu}} \frac{\bar{\mu}}{\sqrt{1-\bar{\mu}^4}}\ \mathrm{sign}\left(\bar{\mu}'\right)\ \mathrm{d}\bar{\mu} \tag{40}$$

We now integrate equation (40) by parts. To this end, let us define

$$I(\bar{\mu}) = \int_0^{\bar{\mu}} \frac{\bar{\mu}}{\sqrt{1-\bar{\mu}^4}}\mathrm{d}\bar{\mu} = \frac{1}{2}\ \arcsin\left(\bar{\mu}^2\right). \tag{41}$$

Therefore,

$$\beta = \arcsin\left(\bar{\mu}^2\right)\ \mathrm{sign}\left(\bar{\mu}'\right) + 2\int_0^{\bar{\mu}} I(\bar{\mu})\,\frac{\mathrm{d}\,\mathrm{sign}\left(\bar{\mu}'\right)}{\mathrm{d}\bar{\mu}}\mathrm{d}\bar{\mu} \tag{42}$$

The derivative of the sign of $\bar{\mu}'$ with respect to $\bar{\mu}$ is a sum of Dirac delta functions, centred in $\bar{\mu} = -1$ (where $\bar{\mu}'$ goes from negative to positive), and $\bar{\mu} = 1$ (where $\bar{\mu}'$ goes from positive to negative).

$$\frac{\mathrm{d}\,\mathrm{sign}(\bar{\mu}')}{\mathrm{d}\bar{\mu}} = 2\sum -\delta(\bar{\mu}-1) + \delta(\bar{\mu}+1). \tag{43}$$

We notice that $I(\pm 1) = \pi/4$. Therefore,

$$\beta(\bar{S}) = \arcsin\left(\bar{\mu}^2\right)\ \mathrm{sign}\left(\bar{\mu}'\right) + \pi\ \left(n_\downarrow(\bar{S}) - n_\uparrow(\bar{S})\right), \tag{44}$$

where $n_\downarrow(\bar{S})$ is the number of times μ' changes sign *from positive to negative* between 0 and $\bar{S}$, while $n_\uparrow(\bar{S})$ is the number of times μ' changes sign *from negative to positive*.

A.3. Deformation

With boundary condition $x(1) = 1$ and $y(1) = 0$, the coordinates of the deformed configuration are given by

$$\begin{aligned} x(S) &= 1 + \int_1^S \cos\theta(S)\,\mathrm{d}S \\ &= 1 - \int_0^1 \cos\theta(S)\,\mathrm{d}S + \int_0^S \cos\theta(S)\,\mathrm{d}S, \end{aligned} \tag{45a}$$

$$\begin{aligned} y(S) &= \int_1^S \sin\theta(S)\,\mathrm{d}S \\ &= -\int_0^1 \sin\theta(S)\,\mathrm{d}S + \int_0^S \sin\theta(S)\,\mathrm{d}S \end{aligned} \tag{45b}$$

We notice that

$$\begin{aligned} \cos\theta &= \cos\beta_1\cos\beta + \sin\beta_1\sin\beta, \\ \sin\theta &= \sin\beta_1\cos\beta - \cos\beta_1\sin\beta. \end{aligned} \tag{46}$$

Moreover,

$$\begin{aligned} \cos\beta(S) &= (-1)^{n_\downarrow - n_\uparrow}\ \cos\left(\bar{\mu}^2\right), \\ \sin\beta(S) &= (-1)^{n_\downarrow - n_\uparrow}\ \mathrm{sign}\left(\bar{\mu}'\right)\ \bar{\mu}^2 = \bar{\mu}^2, \end{aligned} \tag{47}$$

where we used $(-1)^{n_\downarrow - n_\uparrow}\ \mathrm{sign}\left(\bar{\mu}'\right) = 1$ if $Q_0 > 0$.

Hence, using Eq. (36)

$$\begin{aligned} \int_0^S \cos\beta(S)\mathrm{d}S = I_{c\beta} &= S_{\max}\int_0^{\bar{S}} \cos\beta(S)\mathrm{d}\bar{S} \\ &= \sqrt{\frac{2}{Q_0}}\int_0^{\bar{\mu}}, \frac{\cos\arcsin\bar{\mu}^2}{\sqrt{1-\bar{\mu}^4}}\mathrm{d}\bar{\mu} = \sqrt{\frac{2}{Q_0}}\,\bar{\mu} \end{aligned} \tag{48}$$

$$\begin{aligned} \int_0^S \sin\beta(S)\mathrm{d}S = I_{s\beta} &= S_{\max}\int_0^{\bar{S}} \sin\beta(S)\mathrm{d}\bar{S} \\ &= \sqrt{\frac{2}{Q_0}}\int_0^{\bar{\mu}} \mathrm{sign}\left(\bar{\mu}'\right)\ \frac{\bar{\mu}^2}{\sqrt{1-\bar{\mu}^4}}\mathrm{d}\bar{\mu}. \end{aligned} \tag{49}$$

Let us define

$$I_\beta(S) = \int_0^{\bar{\mu}} \frac{\bar{\mu}^2}{\sqrt{1-\bar{\mu}^4}}\mathrm{d}\bar{\mu} = E(\arcsin\bar{\mu}\mid -1) - F(\arcsin\bar{\mu}\mid -1), \tag{50}$$

where E is the *elliptic integral of the second kind* and F is the *elliptic integral of the first kind*. Then,

$$\begin{aligned} I_{s\beta} &= \int_0^S \sin\beta(S)\mathrm{d}S \\ &= \sqrt{\frac{2}{Q_0}}\ \left(\mathrm{sign}\left(\bar{\mu}'\right)\ I_\beta(S) + 2\,I_\beta(1)\ \left(n_\downarrow + n_\uparrow\right)\right), \end{aligned} \tag{51}$$

where and $I_{s\beta}(1) \approx 0.5991$.

Appendix B. Estimation of the transverse thrust provided by the air flow

The transverse follower force, acting at the end of the beam, was provided via the air thrust. This force, linked to the Newton's third low, is generated by the reaction applied to the beam by the accelerating air flowing from the small circular void present at the top of the beam. In this section, the thrust as a function of the measured pressure is derived for the experimental problem schematised in Fig. 6a. Such expression is obtained by applying the *continuity equation*, the *momentum equation* and the *energy equation* to each Control Volume Element (CVE) reported in Fig. 6a.

Momentum equation. With reference to a generic CVE_i defined by the control sections CS_{inlet} and CS_{exit} the momentum equation writes

$$\sum_{\mathrm{CVE}_i} \mathbf{F} = \sum_{\mathrm{CVE}_i} \mathbf{F_{body}} + \sum_{\mathrm{CVE}_i} \mathbf{F_{surface}} = \sum_{CS_{exit}} \beta\dot{m}\mathbf{v} - \sum_{CS_{inlet}} \beta\dot{m}\mathbf{v}, \tag{52}$$

where β is a correction factor (for turbulent flows can be assumed $\simeq$ 1), $\dot{m}$ is the mass flow, $\mathbf{v}$ the velocity and $\sum\mathbf{F}$ the sum of all the body forces and the surface forces acting on the CVE at a particular instant in time.

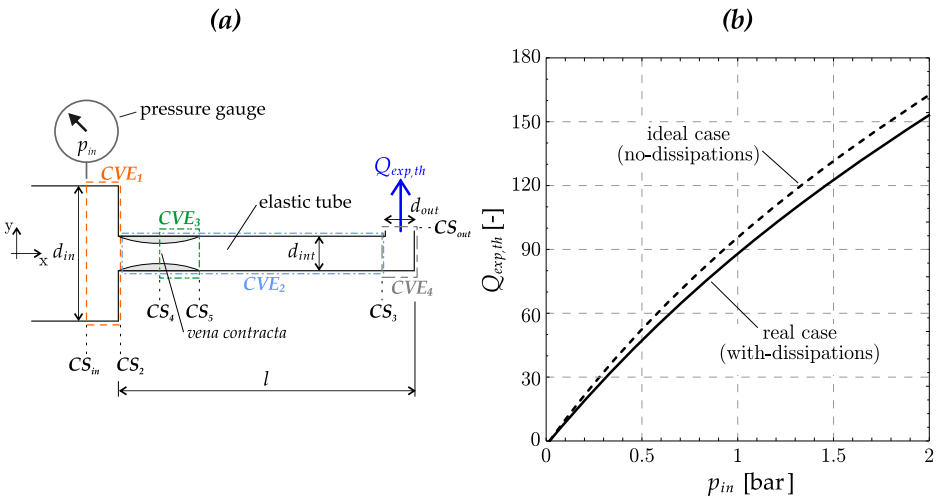

Fig. 6. (a) Scheme of the thrust problem. (b) Transversal dimensionless follower force $Q_{exp,id}$ acting at the top of the beam as a function of the pressure p_0 recorded during the experiments for the ideal case (black/dashed line) and the real case with dissipations (continuous/black line).

Continuity equation. The conservation of the mass flow $\dot{m}$ (continuity equation) through each cross section CS_i can be expressed as

$$\dot{m} = A_i\,\rho_i\,V_i = const, \quad \forall i \in \mathbb{N}, \tag{53}$$

where A_i is the cross section area, ρ_i is the air density and V_i the air velocity. Since the air, assumed dry, is a compressible fluid its density is not constant but depends on pressure and temperature accordingly with the following equation

$$\rho(p,T) \simeq \rho_{dry}(p,T) = \frac{p}{R_{spec}T}, \tag{54}$$

where T is the absolute temperature [K], p the absolute pressure [Pa], R_{spec} = 287.058 [J/(kg K)] the specific gas constant for dry air. For adiabatic and isoentropic compression/expansion processes of an ideal gas the relations among its temperature T, pressure p and density ρ are

$$p^{1-\gamma}T^{\gamma} = const, \quad \frac{\rho}{p^{1/\gamma}} = const, \tag{55}$$

where γ is the heat capacity ratio C_p/C_v. Such a ratio is $\gamma = 7/5$ for air.

Energy equation. In the case of a steady flow with no shaft work, negligible change in elevation and that takes place adiabatically, the energy balance (first low of thermodynamic) reduces to

$$h + \frac{V^2}{2} = h_0 \tag{56}$$

where V is the speed flow and h is enthalpy of the system and h_0 is stagnation (or total) enthalpy.

The enthalpy, equal to the internal energy u plus the product of its pressure p, and its volume V, can be expressed as a function of the heat capacity ratio, the pressure and the density as

$$dh = c_p dT \quad \Rightarrow \quad h = \frac{\gamma}{\gamma-1}\frac{p}{\rho} \tag{57}$$

Therefore, the energy balance low can be written as

$$\frac{V^2}{2} + \frac{\gamma}{\gamma-1}\frac{p}{\rho} = h_0, \tag{58}$$

or equivalently in terms of the mass flow $\dot{m}$ as

$$\frac{\dot{m}^2}{2\,(\rho A)^2} + \frac{\gamma}{\gamma-1}\frac{p}{\rho} = h_0. \tag{59}$$

B.1. Air flow with friction

This subsection is devoted to the estimation of the pressure drop between the corss sections CS_2 and CS_3, namely along the Silicon tube, caused by wall friction (Fanno flow) [42–44]. In the case of a compressible fluid, such as air, and high speed flow the wall friction is usually negligible for short ducts with big cross-sectional area. On the contrary, frictional losses are not negligible for long duct with small cross-sectional area. To correctly take into account wall friction it is convenient rewrite the *momentum equation* in its differential form

$$dp + \frac{\delta F_{friction}}{A} + \rho v dv = 0. \tag{60}$$

In the previous equation, $\delta F_{friction}$ is the friction force that is generated between the inner surface of the duct and the flowing fluid. Such a force is defined as

$$\delta F_{friction} = \rho V^2 \frac{f}{2}\frac{A}{D_h}dx, \tag{61}$$

where f is the friction factor and D_h the hydraulic diameter of the duct; in the case of circular duct $D_h = d$. The friction factor f can be evaluated via the following relation, known as the Colebrook equation

$$\frac{1}{f} = -2.0\log\left(\frac{\varepsilon/D}{3.7} + \frac{2.51}{\mathrm{Re}\sqrt{f}}\right), \tag{62}$$

where $\mathrm{Re} = V_{avg}D/\nu$ is the Reynolds number (V_{avg} is the average flow velocity, $\nu = \mu/\rho$ the kinematic viscosity of the fluid, for air $\nu \approx 10^{-5}$ m^2/s) and ε the roughness of the tube. For the specific case of a Silicon surface, ε is about 0.2–0.3 nm. In the case of compressible fluid flow, it is instrumental to define the variation of the flow properties in terms of the Mach number, $\mathrm{Ma} = V/\sqrt{\gamma R_{spec}T}$, that defines flow regimes. For instance, the flow is sonic when Ma=1, subsonic when Ma<1 and supersonic when Ma>1. In our experiments, the flow regime is always subsonic (Ma<1). The pressure drop along the tube can be computed knowing the flow Mach number at the inlet cross section CS_2 (Ma_2) and at the exit cross section CS_3 (Ma_3), as

$$\Delta P_{friction} = P_2 - P_3 = P_2\left[1 - \frac{\frac{1}{\mathrm{Ma}_3}\left(\frac{k+1}{2+(k-1)\mathrm{Ma}_3^2}\right)^{1/2}}{\frac{1}{\mathrm{Ma}_2}\left(\frac{k+1}{2+(k-1)\mathrm{Ma}_2^2}\right)^{1/2}}\right]. \tag{63}$$

B.2. Sudden contraction of the flow area

The effect of the sudden contraction of the flow area between the cross sections CS_{in} and CS_5 has been evaluated accordingly with the procedure reported in the work [45]. In the case of a compressible fluid, the dissipation due to sudden changes in the flow area are usually considered "minor losses". The pressure losses are assumed to be negligible from CS_{in} to the *vena contracta* CS_4 while they can cause an entropy increase from the *vena contracta* (CS_4) to CS_5. The pressure drop $\Delta P_{contraction}$ is determined by applying the *continuity equation*, the *momentum equation* and the *energy equation* to the CVE_3 considering an effective flow area at the *vena contracta* $A_4 = C_d A_{int}$, smaller than that of the duct, $A_{int} = \pi d_{int}^2/4$. The steady flow discharge coefficient C_d, function of the area contraction (A_{in}/A_{int}) and of the pressure drop (P_{in}/P_4), is defined as

$$C_d = 1.02\frac{P_{in}}{P_4} - 0.36\left(\frac{P_{in}}{P_4}\right)^2. \tag{64}$$

B.3. Thrust acting at the top the beam

The thrust **P** acting at top of the beam can be derived from the momentum equation applied on CVE_4 as

$$\mathbf{P} = \sum \mathbf{F} = \sum_{CS_{out}} \beta \dot{m}\mathbf{v} - \sum_{CS_{in}} \beta \dot{m}\mathbf{v} \tag{65}$$

where β is a correction factor (for turbulent flows can be assumed $\simeq 1$), $\dot{m}$ is the mass flow and **v** the velocity.

Being $p_{out} \simeq p_{atm}$, the transverse follower force F, equal to the component of the air thrust S along the y axis can be expressed as

$$Q_{exp,th} = P_y \simeq \rho_{atm} A_{out} v_{out}^2, \tag{66}$$

where ρ_{atm} = 1.204 kg/m^3 is the air density at 20 °C and at 101.325 kPa, $A_{out} = \pi d_{out}^2/4$ the area of the void at the top of the beam and d_{out} its diameter.

By applying Eqs. (66), (53) and (59) on each control sections CS_i reported in Fig. 6a it is possible to obtain the analytical equation that provides the mass flow $\dot{m}$.

Finally, note $\dot{m}$ from the above equation, the transversal follower force $Q_{exp,id}$ generated by the air flow and the pressure p_{in} recorded during the experiments is

$$Q_{exp,th} = \frac{\dot{m}^2}{\rho_{out} A_{out}} \tag{67}$$

In Fig. 6b is reported the dimensionless transversal follower force $Q_{exp,th}$ as a function of the pressure p_0 measured during the experiments for the ideal case (no-dissipations, black/dashed line) and the real case (with dissipations, blue/continuous line). The curves are obtained replacing each parameter with the actual value of the experiments accordingly with those reported in Section 4.

B.3.1. Ideal case (no-dissipations)

For the ideal case of no-dissipations (frictionless tube and negligible effect of the sudden change of area between the cross sections CS_{in} and CS_5) the mass flow $\dot{m}$ can be determined through the closed-form expression

$$\dot{m} = \sqrt{\frac{2\gamma}{\gamma - 1}\left(\frac{p_{in}}{\rho_{in}} - \frac{p_{atm}}{\rho_{atm}}\right)\left(\frac{1}{\rho_{atm}^2 A_{out}^2} - \frac{1}{\rho_{in}^2 A_{in}^2}\right)^{-1}}. \tag{68}$$

The previous expression has been obtained by applying the *continuity equation*, the *momentum equation* and the *energy equation* on cross sections CS_{in} and CS_{out}.

B.3.2. Real case (with dissipations)

In the event that the effect of the wall friction and the sudden contraction of the flow area are not neglected, the mass flow cannot be determined via a closed-form expression as in the ideal case. For this purpose, a specific algorithm has been written in *Mathematica* to compute iteratively the mass flow known the pressure p_0 recorded during the experiments. For each pressure p_{in}, the code determines the mass flow $\dot{m}_{diss}$ with all the sources of dissipation, as shown in Appendices B.1 and B.2, assuming as a mass flow of the first-attempt that provided by Eq. (68) for the ideal case. The condition $e^{(k)} = (\dot{m}_{diss}^{(k)} - \dot{m}_{diss}^{(k-1)})/\dot{m}_{diss}^{(k)} < 0.001$ on the residual error has been assumed as termination criteria for the iterative procedure (k represents the iteration step). The value of $\dot{m}_{diss}^{(k)}$ for which such a condition is matched represents the mass flow for the real case with dissipation.

Appendix C. Supplementary data

Supplementary material related to this article can be found online at https://doi.org/10.1016/j.eml.2020.101110.

References

[1] I. Elishakoff, Controversy associated with the so-called "follower forces": critical overview, Appl. Mech. Rev. 58 (2) (2005) 117–142.
[2] A. Samantaray, R. Bhattacharyya, A. Mukherjee, On the stability of Crandall gyropendulum, Phys. Lett. A 372 (3) (2008) 238–243.
[3] J. Kooijman, J.P. Meijaard, J.M. Papadopoulos, A. Ruina, A. Schwab, A bicycle can be self-stable without gyroscopic or caster effects, Science 332 (6027) (2011) 339–342.
[4] L. Pigolotti, C. Mannini, G. Bartoli, K. Thiele, Critical and post-critical behaviour of two-degree-of-freedom flutter-based generators, J. Sound Vib. 404 (2017) 116–140.
[5] S. Mandre, L. Mahadevan, A generalized theory of viscous and inviscid flutter, Proc. R. Soc. A 466 (2113) (2009) 141–156.
[6] M.A. Karami, D.J. Inman, Equivalent damping and frequency change for linear and nonlinear hybrid vibrational energy harvesting systems, J. Sound Vib. 330 (23) (2011) 5583–5597.
[7] S. Aoi, Y. Egi, K. Tsuchiya, Instability-based mechanism for body undulations in centipede locomotion, Phys. Rev. E 87 (1) (2013) 012717.
[8] G. Salussolia, E. Barbieri, N.M. Pugno, L. Botto, Micromechanics of liquid-phase exfoliation of a layered 2D material: A hydrodynamic peeling model, J. Mech. Phys. Solids 134 (2020) 103764.
[9] A. Rohlmann, T. Zander, M. Rao, G. Bergmann, Applying a follower load delivers realistic results for simulating standing, J. Biomech. 42 (10) (2009) 1520–1526.
[10] P. Bayly, S. Dutcher, Steady dynein forces induce flutter instability and propagating waves in mathematical models of flagella, J. R. Soc. Interface 13 (123) (2016) 20160523.
[11] G. De Canio, E. Lauga, R.E. Goldstein, Spontaneous oscillations of elastic filaments induced by molecular motors, J. R. Soc. Interface 14 (136) (2017) 20170491.
[12] S. Chandrasekhar, On stars, their evolution and their stability, Rev. Modern Phys. 56 (2) (1984) 137.
[13] O.N. Kirillov, Singular diffusionless limits of double-diffusive instabilities in magnetohydrodynamics, Proc. R. Soc. A 473 (2205) (2017) 20170344.
[14] O.N. Kirillov, Nonconservative Stability Problems of Modern Physics, Vol. 14, Walter de Gruyter, 2013.
[15] M. Berry, P. Shukla, Hamiltonian curl forces, Proc. R. Soc. A 471 (2176) (2015) 20150002.
[16] M. Berry, P. Shukla, Curl force dynamics: symmetries, chaos and constants of motion, New J. Phys. 18 (6) (2016) 063018.
[17] A. Pflüger, Stabilitätsprobleme der Elastostatik, Springer-Verlag, 1950.
[18] A. Pfluger, To stabilize ' the tangential bar, ZAMM J. Appl. Math. Mech. 35 (5) (1955) 191.
[19] M. Tommasini, O.N. Kirillov, D. Misseroni, D. Bigoni, The destabilizing effect of external damping: Singular flutter boundary for the Pflüger column with vanishing external dissipation, J. Mech. Phys. Solids 91 (2016) 204–215.
[20] D. Bigoni, D. Misseroni, M. Tommasini, O.N. Kirillov, G. Noselli, Detecting singular weak-dissipation limit for flutter onset in reversible systems, Phys. Rev. E 97 (2) (2018) 023003.
[21] H. Ziegler, Die stabilitätskriterien der elastomechanik, Arch. Appl. Mech. 20 (1) (1952) 49–56.
[22] H. Ziegler, On the concept of elastic stability, in: Advances in Applied Mechanics, Vol. 4, Elsevier, 1956, pp. 351–403.

[23] O. Bottema, The Routh-Hurwitz condition for the biquadratic equation, Indag. Math. (N.S.) 18 (1956) 403–406.
[24] H. Ziegler, Principles of Structural Stability, Vol. 35, Birkhäuser, 1977.
[25] D. Bigoni, O.N. Kirillov, D. Misseroni, G. Noselli, M. Tommasini, Flutter and divergence instability in the Pflüger column: Experimental evidence of the Ziegler destabilization paradox, J. Mech. Phys. Solids 116 (2018) 99–116.
[26] M. Beck, The buckling load of the unilaterally clamped, tangentially pressed rod, J. Appl. Math. Phys. ZAMP 3 (3) (1952) 225–228.
[27] V. Reut, About the theory of elastic stability, Proc. Odessa Inst. Civ. Communal Eng. 1 (1939) 126–138.
[28] D. Bigoni, D. Misseroni, Structures loaded with a force acting along a fixed straight line, or the "Reut's column problem", J. Mech. Phys. Solids 134 (2020) 103741.
[29] V.V. Bolotin, Nonconservative Problems of the Theory of Elastic Stability, Macmillan, 1963.
[30] G. Herrmann, S. Nemat-Nasser, S. Prasad, Models Demonstrating Instability of Non-Conservative Mechanical Systems, Northwestern University Structural Mechanics Laboratory Technical Report 66–4, 1966.
[31] W. Wood, S. Saw, P. Saunders, The kinetic stability of a tangentially loaded strut, Proc. R. Soc. Lond. Ser. A Math. Phys. Eng. Sci. 313 (1513) (1969) 239–248.
[32] Y. Sugiyama, K. Katayama, S. Kinoi, Flutter of cantilevered column under rocket thrust, J. Aerosp. Eng. 8 (1) (1995) 9–15.
[33] Y. Sugiyama, M. Langthjem, B. Ryu, Realistic follower forces, J. Sound Vib. 225 (4) (1999) 779–782.
[34] Y. Sugiyama, K. Katayama, K. Kiriyama, B.-J. Ryu, Experimental verification of dynamic stability of vertical cantilevered columns subjected to a sub-tangential force, J. Sound Vib. 236 (2) (2000) 193–207.
[35] D. Bigoni, G. Noselli, Experimental evidence of flutter and divergence instabilities induced by dry friction, J. Mech. Phys. Solids 59 (10) (2011) 2208–2226.
[36] M. Batista, Analytical treatment of equilibrium configurations of cantilever under terminal loads using Jacobi elliptical functions, Int. J. Solids Struct. 51 (13) (2014) 2308–2326.
[37] E. Barbieri, Analytical solution of the cantilevered elastica subjected to a normal, uniformly distributed follower load, Int. J. Solids Struct. (2020).
[38] D. Bigoni, Nonlinear Solid Mechanics: Bifurcation Theory and Material Instability, Cambridge University Press, 2012.
[39] D. Bigoni, Flutter from friction in solids and structures, in: Dynamic Stability and Bifurcation in Nonconservative Mechanics, Springer, 2019, pp. 1–61.
[40] R. Frisch-Fay, Flexible Bars, Butterworths, 1962.
[41] S. Antman, General solutions for plane extensible elasticae having nonlinear stress-strain laws, Quart. Appl. Math. 26 (1) (1968) 35–47.
[42] Y.A. Cengel, J.M. Cimbala, Fluid Mechanics - Fundamentals and Applications, McGraw-Hill series in mechanical engineering, 2013.
[43] F.M. White, Fluid Mechanics, McGraw-Hill Education, 2017.
[44] A.H. Shapiro, The Dynamics and Thermodynamics of COMPRESSIBLE FLUID FLOW, John Wiley & Sons, 1953.
[45] G. Trengrouse, M. Soliman, Effect of sudden changes in flow area on pressure waves of finite amplitude, J. Mech. Eng. Sci. 8 (2) (1966) 198–206.